Lab on a Chip

PAPER

View Article Online
View Journal | View Issue

Cite this: *Lab Chip*, 2025, **25**, 5506

Open Access Article. Published on 04 August 2025. Downloaded on 6/16/2026 10:50:35 PM.
This article is licensed under a Creative Commons Attribution-NonCommercial 3.0 Unported Licence.

Programmable 3DP microfluidic bio-reaction system: automated LAMP-on-a-chip

M. Tugrul Birtek,[a] Nazente Atceken[abc] and Savas Tasoglu*[acdefg]

Point-of-care (PoC) devices have revolutionized healthcare by enabling remote diagnostics and therapeutics, with microfluidic systems playing a pivotal role in their advancement. This study focuses on the detailed engineering and characterization of three-dimensional hydrophobic valves to form novel programmable bio-reaction reservoirs. Using 3D-printed soft lithography, we meticulously investigated the effects of channel dimensions and surface properties on the burst pressures of these reservoirs, which ranged from 6.4 to 44.8 mbar. The bio-reaction reservoirs were demonstrated in both series and parallel configurations, offering versatile platforms for the miniaturization and automation of biological processes. Our findings highlight the capability of these reservoirs to program flows in a variety of fluid samples, including water, blood and serum. Additionally, a portable pressure pump was developed to leverage the functionality of these hydrophobic valves, enabling precise control of fluid dynamics in PoC applications. The study culminated in the design of a microfluidic chip integrating two consecutive reservoirs for the PoC execution of loop-mediated isothermal amplification (LAMP) for detection of the Mpox virus. Primers were lyophilized within the bio-reservoirs, and the system successfully enabled visible colorimetric detection *via* the LAMP assay.

Received 3rd January 2025,
Accepted 4th August 2025

DOI: 10.1039/d5lc00003c

rsc.li/loc

1. Introduction

Point-of-care (PoC) devices have transformed the healthcare industry by facilitating remote diagnostics and therapeutics.[1,2] Microfluidic tools have a crucial role in these systems for precise and programmable control of fluids and micro/nanoparticles.[3–5] The integration of microfluidic structures has significantly advanced precision medicine through a range of biomedical applications including proteomic and genetic analyses, cell culture and drug screening platforms.[6–10] Precise manipulation of fluids at micron level requires detailed investigation of low Re flow regimes, which are governed by viscous and surface tension forces.[11,12] Designing microfluidic circuits analogous to sensitive electronic circuits is essential for addressing these challenges.[13,14]

Microfluidic valves and logical operators are widely utilized for automated execution of biological and chemical processes.[15–21] Active valves exploit external force fields to enable realization of logical switching operations in microfluidic circuits.[22–24] Electronic transistor functions such as regulation, amplification and latching can be effectively mimicked in the microfluidic realm.[25] Passive valves, primarily relying on capillary phenomena, ease the fluidic programming without requiring external stimulation and related equipment.[26] Hydrophilic valves can be used to devise self-pumping logic circuits.[27] Likewise, hydrophobic valves enable concurrent recognition of various compounds in a sample from a single inlet.[15,28] However, conventional soft lithography has limited the development of hydrophobic valves since achieving channel shrinkage in three dimensions poses challenges.[29–31] The advent of additive manufacturing in microfluidic valve fabrication has empowered engineering of automated microfluidic platforms that consecutively perform separation, amplification and recognition of disease related nucleic acids (NAs) from body fluids.[32] Furthermore, 3D hydrophobic valves can be employed for the development of programmable reaction chambers that can be tailored based on hand pipetting.[33]

The precise operation of these miniature chips still largely relies on bulky and expensive pumps, limiting their deployment in PoC settings.[34] Finger actuation and capillary-drive can enable pumping in remote settings.[35–40] Yet, active

---

[a] *Department of Biomedical Sciences and Engineering, Koç University, Sariyer, Istanbul, Turkey 34450. E-mail: stasoglu@ku.edu.tr*
[b] *School of Medicine, Koç University, Istanbul, 34450, Turkey*
[c] *Koç University Translational Medicine Research Center (KUTTAM), Koç University, Istanbul, Turkey 34450*
[d] *Department of Mechanical Engineering, Koç University, Istanbul, Turkey 34450*
[e] *Koç University Is Bank Artificial Intelligence Lab (KUIS AILab), Koç University, Sariyer, Istanbul, Turkey 34450*
[f] *Koç University Arçelik Research Center for Creative Industries (KUAR), Koç University, Istanbul, Turkey 34450*
[g] *Boğaziçi Institute of Biomedical Engineering, Boğaziçi University, Çengelköy, Istanbul, Turkey 34684*

This journal is © The Royal Society of Chemistry 2025

Open Access Article. Published on 04 August 2025. Downloaded on 6/16/2026 10:50:35 PM. This article is licensed under a Creative Commons Attribution-NonCommercial 3.0 Unported Licence.

pumps, which utilize external force fields, provide superior control over fluid dynamics.[41] Syringe pumps, the most widely used in microfluidics for their robust flow rate control, are cumbersome and unsuitable for pressure-dependent microfluidic systems, limiting their use outside the lab.[42] Because these pumps operate by continuous mechanical displacement, they inherently accumulate pressure at the inlet, making real-time feedback necessary for precise regulation.[43] While they can be cost-effective for flows requiring inlet pressures in the hundreds of mbar, it cannot reliably deliver non-pulsatile pressures with sub-10 mbar resolution. Alternatively, pressure and vacuum-driven pumps provide greater versatility in operating advanced microfluidic systems.[44] In particular, high-resolution (~1 mbar) pressure control can be achieved with pressure pumps, ensuring both precise and accurate regulation of the inlet pressure.[45] However, these pumps are prohibitively expensive and often require large compressors to function, making it impractical to move pressure-controlled microfluidic systems out of the lab and into PoC applications. The development of portable and affordable pressure pumps could revolutionize PoC applications by making advanced microfluidic systems viable in remote settings.[46,47]

In this study, three-dimensional hydrophobic valves were engineered to form programmable bio-reaction reservoirs. The effects of channel dimensions and surface properties on burst pressure of 3D printed reservoirs were meticulously investigated. The operation of reservoirs in series and parallel arrangements were demonstrated, which can facilitate the miniaturization of biological processes. The effectiveness of the valves, with burst pressures that can be precisely engineered up to ~35 mbar, was validated by programming flow of various fluids, including water, blood, and serum.

Additionally, an Arduino-controlled, low-cost and portable pressure pump was developed to enable PoC application of these programmable bio-reaction reservoirs. This battery-

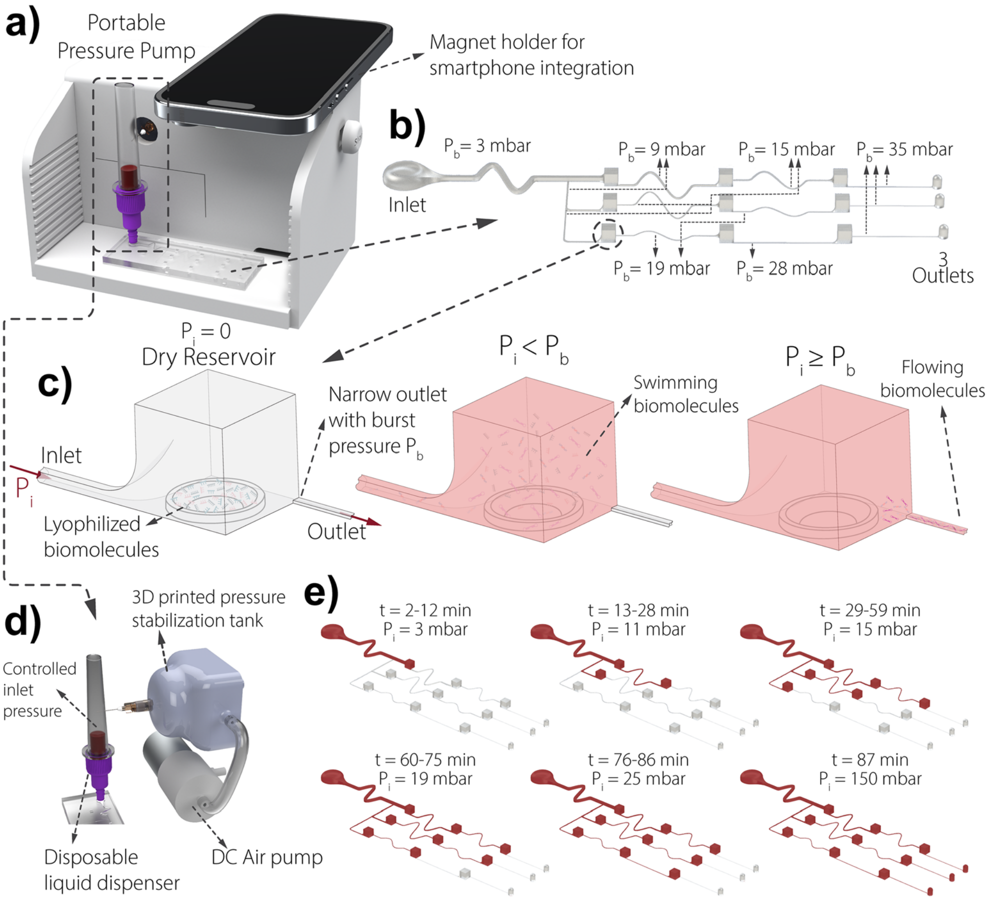

Fig. 1 Demonstrations of portable pressure pump and programmable reaction reservoirs. (a) Render of the portable pressure pump integrating disposable liquid dispenser tubes with the microfluidic chip. The Arduino-controlled, battery-powered pump applies a defined pressure cycle when the start button is pressed. An embedded magnet enables easy smartphone integration for imaging and control. (b) Microfluidic chip featuring a single inlet that splits into three parallel channels, each containing three serially connected reaction reservoirs, totaling nine reservoirs. (c) Illustration of the bio-reaction reservoirs composed of PDMS layers: a top cubic fluid chamber and a bottom layer with a sharp-edged hole for biomolecule immobilization. Fluid is pumped in with inlet pressure P_i. The narrow outlet creates a pressure barrier P_b that must be overcome to wet the channel. The fluid remains inside the reservoir while $P_i < P_b$, rehydrating immobilized molecules, and is pumped out when $P_i > P_b$. (d) The 3D-printed tank has an intrinsic leak to stabilize the pulsatile pressure of the commercial DC air pump. Tank pressure is connected to the dispenser *via* a needle. (e) Automated fluid handling in the serially and parallel-connected microfluidic chip.

Open Access Article. Published on 04 August 2025. Downloaded on 6/16/2026 10:50:35 PM.
This article is licensed under a Creative Commons Attribution-NonCommercial 3.0 Unported Licence.

powered pump could apply air pressure in the range of 3 to 166 mbar to fluids within commercial liquid test tubes that are compatible with microfluidic chips. The accuracy of the applied pressure of the pump was characterized to be ±2 mbar. The pump's capability to automate various hydrophobic valve-based microfluidic structures was demonstrated. The integration of reservoirs with a pressure pump enabled the innovation of time-programmable pump and rest sequences from a single fluid inlet.

Finally, a chip that contains two consecutive reservoirs that enable autonomous execution of loop-mediated isothermal amplification (LAMP)-based PoC detection of Mpox virus was developed. LAMP primers were lyophilized within bio-reservoirs. The sample containing fluid was pumped to the LAMP reservoir and heated with a heating module that is integrated to the portable pump. Following the 30 minutes application of the colorimetric reaction, the fluid was pumped to imaging region. The PoC system was able to detect the Mpox with smart-phone imaging and eye vision.

2. Methods

2.1. Mechanism of the hydrophobic valve-based bio-reaction reservoirs

Hydrophobic valves function by exploiting negative capillary forces that arise from the hydrophobicity of the surrounding material. These forces result from the pressure difference at the interface between two immiscible fluids, driven by the interactions between the fluid molecules and the surface of the confined space.[48] Microfluidic channels are initially filled with the air in most cases. Polydimethylsiloxane (PDMS), the most common material used in microfluidics research, has naturally a hydrophobic surface.[49] Thus, when a PDMS channel is desired to be filled with a liquid, a certain pressure must be applied to wet the surface (eqn (1)). This is generally referred to as burst pressure (P_b) in microfluidic systems.[50]

$$P_b = 2\gamma\left(\frac{\cos\theta}{w} + \frac{\cos\theta}{h}\right) \tag{1}$$

Here, θ, γ, w and h denote the contact angle, surface tension of the liquid, the width and height of the channel, respectively. The fluid does not move through an air filled channel if the applied inlet pressure do not exceed P_b. We utilized this phenomenon by adding narrow outlets to the wider reservoirs along microchannels (Fig. 1b). Controlling the pressure of the liquid at inlet makes the programmable flow possible. For instance, liquid will fill the chamber but not flow outside when the applied pressure is below P_b (Fig. 1c). Increasing the pressure to P_b drives the fluid out of the reservoir. The inlet pressure can be programmed by a computer controlled pressure pump to keep the sample inside this reservoir for a desired time and then pump it to a following microfluidic structure.

2.2. Experimental characterization of reservoirs

3D printed soft lithography was used to manufacture reservoirs with various dimensions (Table 1). The widths of manufactured channels were measured from microscopy images. The heights of the printed channels were measured with Bruker DekTakXT (Germany) surface profilometer. Details and findings related to the manufacturing are thoroughly explained in SI.

Elveflow OB1 pressure pump (Elvesys, France) was used for characterization of the reservoirs and the multiple reservoir systems. The experimental setup for characterization of burst pressures is illustrated in Fig. 2b. The Falcon tubes were filled with 15 mL of distilled water

Table 1 The theoretical and experimental values of 19 characterized outlet channel geometries

Design	CAD width (μm)	CAD height (μm)	Measured width (μm)	Measured height (μm)	Aspect ratio (w/h)	Experimental burst pressure P_{b-exp} (mbar)	Calculated burst pressure P_{b-the} (mbar)	Measured contact angle (°)
40–50	40	50	46.90	37.24	1.26	23.4	23.73	110
40–100	40	100	67.95	80.79	0.84	14.2	13.34	110
80–50	80	50	100.69	45.68	2.20	14.6	15.67	110
80–100	80	100	95.17	83.35	1.14	11.0	11.08	110
80–150	80	150	113.10	126.92	0.89	9.4	8.24	110
200–100	200	100	220.69	85.00	2.60	7.4	8.03	110
100–200	100	200	124.14	164.80	0.75	6.4	6.96	110
100–150	100	150	106.22	126.41	0.84	8.4	8.53	110
100–100	100	100	118.62	86.46	1.37	9.6	9.85	110
100–50	100	50	108.97	48.10	2.27	16.8	14.76	110
20–60	20	60	27.59	38.91	0.71	36.0	30.51	110
40–30	40	30	44.14	17.48	2.53	44.8	39.33	110
40–120	40	120	53.79	75.70	0.71	15.3	15.66	110
60–30	60	30	68.11	21.87	3.11	33.6	29.75	110
120–180	120	180	154.84	114.06	1.36	8.4	8.38	110
120–60	120	60	148.97	45.81	3.25	14.8	14.06	110
120–30	120	30	124.42	27.00	4.61	25.6	22.20	110
60–90	60	90	80.18	62.35	1.29	15.4	14.04	110
80–30	80	30	63.45	21.08	3.01	38.2	31.13	110

This journal is © The Royal Society of Chemistry 2025

Open Access Article. Published on 04 August 2025. Downloaded on 6/16/2026 10:50:35 PM.
This article is licensed under a Creative Commons Attribution-NonCommercial 3.0 Unported Licence.

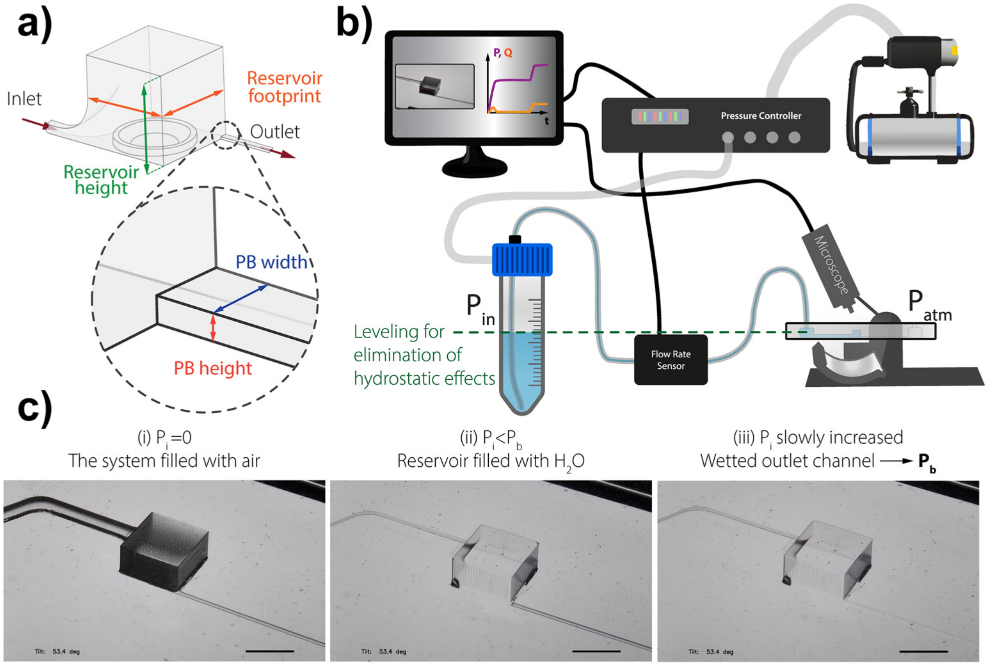

Fig. 2 Explanation of the experimental setup for characterization of burst pressure. (a) Geometrical parameters defining the dimensions of the reservoir. (b) Illustration of the experimental setup used for reservoir characterization: the pressure controller supplies pressure to a Falcon tube holding the liquid, which is transferred to the microfluidic chip through an immersed microtube. The microscope enables real-time observation of fluid movement. (c) Microscope images showing the characterization process: the system is initially filled with air; distilled water is pumped into the reservoir with an inlet pressure P_i below P_b; then, the pressure is slowly increased until wetting of the outlet channel is observed. All scale bars are 1 mm.

and a micro-tube was dipped inside. The other end of the tube was inserted to the inlet of the microfluidic chips. The chips were placed on a Microqubic 3D microscope (Switzerland) for live imaging. The Falcon tubes were leveled with the microfluidic chip to minimize the effect of hydrostatic pressure. The liquid was slowly filled into the reservoir with a pressure below 10 mbar (Fig. 2c). Then the target pressure was set to 1 mbar on the Elveflow interface and waited 1 minute for the stabilization. The pressure was increased at a rate of ~0.06 mbar s^{-1} and the movement of the fluid was observed on the live microscope image. The increase of the pressure was stopped once the fluid started moving in the narrow channel. The pressure was noted as burst pressure after the complete wetting of the narrow channel was observed (Fig. 2c). The flow rate was recorded simultaneously to detect the flow. However, the flow rate was below 0.02 μL min^{-1} which is less than the flow rate sensor sensitivity specified by the company.

2.3. Definitions of characterized parameters

According to eqn (1), the tunability of the burst pressure is possible by changing the channel width (w), height (h) and the contact angle. To verify the practicality of the Young–Laplace equation to design reservoirs with specific P_b values, we created 19 channels with different outlet channel cross-sections (Table 1). The channels possessed the same inlet length, reservoir footprint and height for impartial observation of the effects of width and height of outlet channels. The effect of the contact angle was tested by time dependent tests on same channel design after plasma treatment (Fig. 3b).

The contact angle of the 3D printing based PDMS chips vary depending on the surface roughness and the storage temperature (SI section S2). Two of every tested microfluidic channel in this section were demolded and kept in the same environmental conditions. The chip to be tested was bonded to a flat PDMS layer and the other remained unbound for measurement of the contact angle before experiments.

Potential impacts of reservoir footprint, height on P_b are experimented using the channels depicted in Fig. 3d and e. Square reservoirs with a fixed height of 1.5 mm and varying footprints—with edge lengths ranging from 200 μm to 3 mm—were tested to assess the effect of reservoir footprint (Fig. 3d). Conversely, to assess the effect of reservoir height on P_b, we varied the heights of reservoirs with a fixed footprint of 1.5 × 1.5 mm from 250 μm to 1.5 mm (Fig. 3e).

$$\mathrm{Ca} = \frac{\mu U}{\gamma} \tag{2}$$

The balance between capillary forces and viscous forces in a flow is quantified by the capillary number (eqn (2)), where μ, γ and U represent dynamic viscosity, surface tension, and flow velocity, respectively. In a single reservoir, capillary forces prevail because the fluid velocity U reaches to zero (Ca = 0). However, when fluid starts flowing through the outlet

Open Access Article. Published on 04 August 2025. Downloaded on 6/16/2026 10:50:35 PM.
This article is licensed under a Creative Commons Attribution-NonCommercial 3.0 Unported Licence.

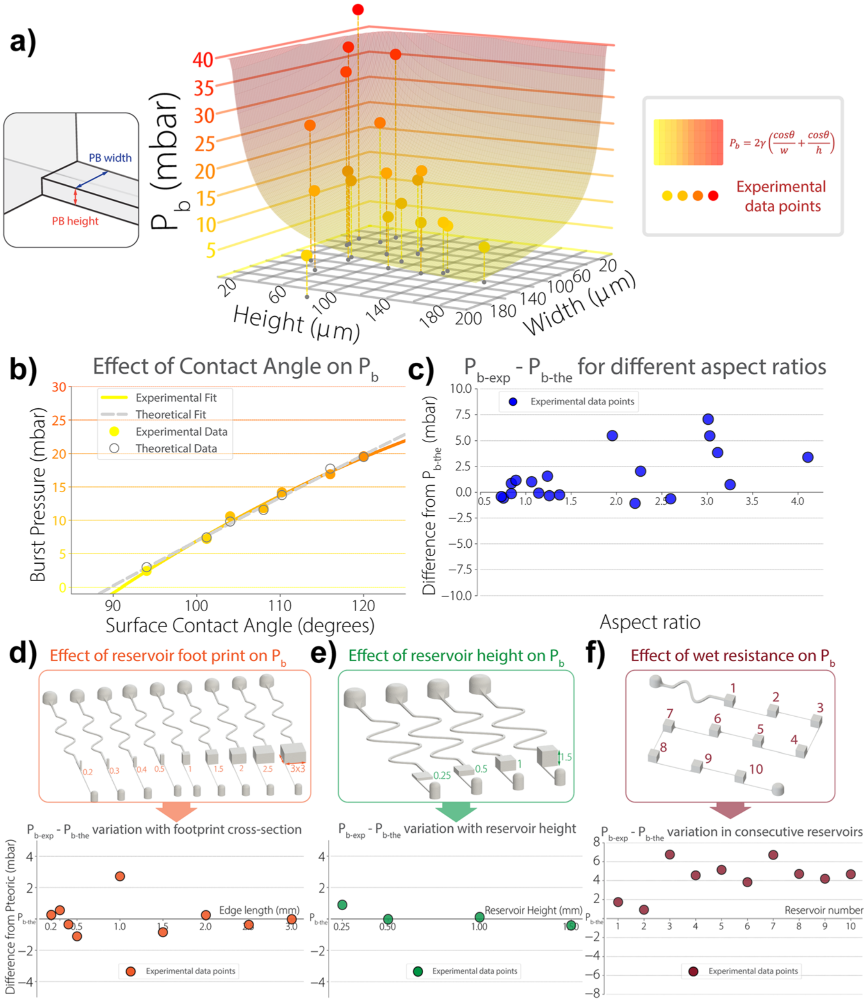

Fig. 3 Analyses of burst pressure through comparison of experimental data and theoretical predictions. (a) Comparison of experimentally calculated $P_{b\text{-exp}}$ with $P_{b\text{-the}}$ calculated with eqn (1). The transparent surface with varying color shows the theoretical values while the opaque scatter points indicate experimental data points. (b) Effect of the contact angle on P_b. The plot was generated by experimenting with the same channel design at different time steps after plasma treatment. (c) Efficiency of eqn (1) for different aspect ratios. The experimental dataset in (a) was used for creating this plot. The horizontal axis is equal to $P_{b\text{-the}}$ and the vertical axis shows the subtraction of it from $P_{b\text{-exp}}$. Differences are consistently minimized for aspect ratios below 2 and randomly distributed for greater aspect ratios. (d–f) Investigation of the effect of reservoir geometry and hydrodynamic resistance on burst pressure. Difference between experimentally measured burst pressure and calculated burst pressure for reservoirs with (d) varying footprint cross-sections and (e) varying reservoir heights. The findings indicate that there is not a limitation for these dimensions and the reservoir volume can adjusted according to reactions. (f) Examination of whether hydrodynamic resistance affects the burst pressure in consecutively connected reservoirs of identical dimensions. All channels between the reservoirs were designed with the same geometrical values.

channel, viscous forces may become effective, leading to hydrodynamic resistance. To determine whether this added resistance should be considered in the design process, we designed a microfluidic channel comprising ten serially connected reservoirs of identical dimensions (Fig. 3f) to assess the impact of increased hydrodynamic resistance on the system's performance.

2.4. Design and characterization of the microfluidic chip with nine reservoirs arranged in three parallel chains

The microfluidic chip shown in Fig. 1b was designed to demonstrate the use of reaction reservoirs in both serial and parallel configurations. P_bs of the reservoirs were tailored to manipulate the fluid in a specific sequence. The reservoirs are numbered sequentially according to their order in the flow path: 1; 2–1 and 2–2; 3–1, 3–2, 3–3; 4–1, 4–2; and 5 (Fig. 4b). Initially, the fluid was pumped into the reservoir 1 and held there for 10 minutes. Then, the pressure was increased to move the fluid into the reservoirs 2–1 and 2–2, where it remained for another 15 minutes. Further increasing the pressure allowed the fluid to reside in reservoirs 3–1, 3–2 and 3–3 for 30 minutes. Subsequently, the fluid was pumped into reservoirs 4–1 and 4–2 for 15 minutes, and finally into reservoir 5 for the last 10 minutes. At the end of the sequence, the pressure was

Open Access Article. Published on 04 August 2025. Downloaded on 6/16/2026 10:50:35 PM.
This article is licensed under a Creative Commons Attribution-NonCommercial 3.0 Unported Licence.

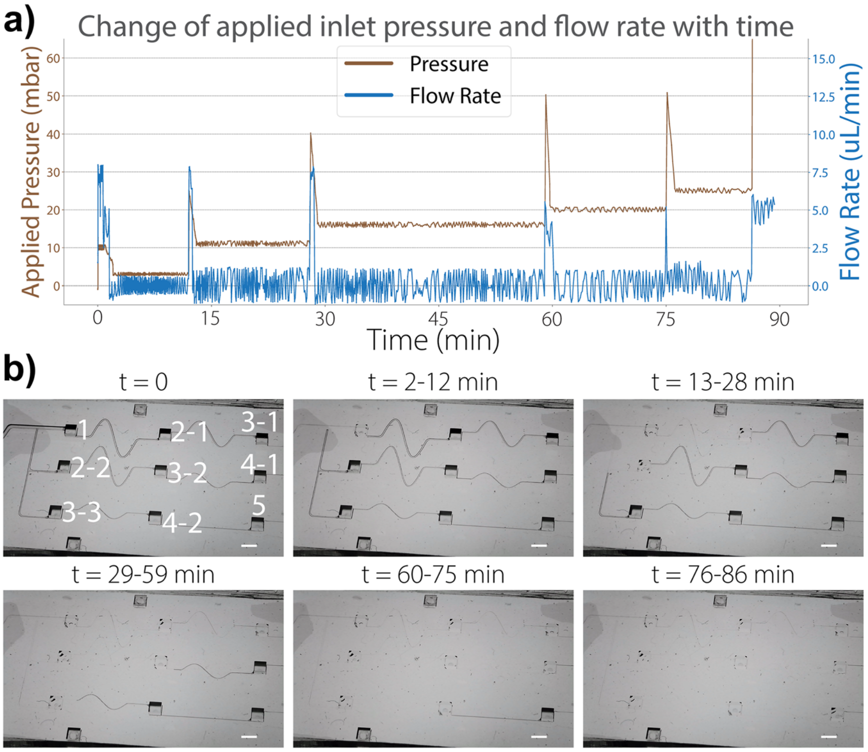

Fig. 4 Operation of the microfluidic chip with nine reservoirs arranged in three parallel chains, using the Elveflow pressure controller. (a) Graph showing the applied pressure and the measured flow rate into the system over time. (b) Microscopy images of the chip at specified times. Microscopy images of the chip at specified times. At *t* = 0, the system is filled with air. The reservoirs are consecutively filled with water at the desired times by applying the pressure cycle depicted in the graph. The reservoirs become hardly noticeable when filled with water due to the transparency of the fluid. The flow rate is recorded simultaneously with the pressure application. Reservoirs are numbered according to flow order on *t* = 0 image. Scale bars 2 mm.

set to 150 mbar to pump the fluid out through the three outputs.

Fig. 4 and Video S1 show the experimental procedure for testing this design. As with all the microfluidic chips tested, the surface contact angle of a twin, unbonded PDMS chip was measured, and the geometrical values and surface contact angles are listed in Table 3. Using these data, eqn (1) was employed to calculate the P_b of each reservoir. A python script was used to automatically control the P_i supplied by the pressure pump. The applied pressure and the flow rate through the system were recorded simultaneously with the video recording.

Following the experimentation with the Elveflow pressure controller, the chip was used with portable pressure pump for facilitating PoC flow automation (Fig. 5d). Blue food color was added to water for improved visibility. Immunosuppressants CRM in human whole blood (K2EDTA) solution (I-507, Cerilliant) and human serum (H4522, Sigma-Aldrich) were purchased and used as received in flow tests.

2.5. Design and characterization of the portable pressure pump

The commercial mini aquarium air pump used to pressurize air was purchased from a local electronics store. The commercial air pump device converts DC electrical power into air pressure through rotary peristaltic compression. The air tank depicted in Fig. 1d serves as a pressure stabilizer and features an inlet and an outlet. A syringe needle, attached to the outlet of the tank, was used to pierce and connect to the disposable liquid dispenser that holds the fluid to be pumped.

The pump body is engineered with integrated mounting slots that facilitate easy attachment of custom-designed modules. A magnet placed on top of the pump body enables easy coupling with a smartphone for control and monitoring purposes. Detailed information about the pump design, manufacturing and electronic system is provided in the SI section S7. To control the pressure pump instantaneously, a GUI was developed with open-source processing software sketchbook (Fig. S11b). The CAD files of the device and the scripts of the GUI are available on our lab repository.

To characterize the pressure output of the pump, we employed a U-shaped microfluidic channel (Fig. 5b). It was designed with two inlets: one connected to a pressure controller and the other to our pump. Before starting the pressure characterization, we pipetted 300 μL of lubrication oil into the channel to serve as a visual indicator of pressure balance. Initially, the system was characterized by using a DC

Open Access Article. Published on 04 August 2025. Downloaded on 6/16/2026 10:50:35 PM.
This article is licensed under a Creative Commons Attribution-NonCommercial 3.0 Unported Licence.

Table 2 Results of the tests for effects of reservoir geometry and hydrodynamic resistance on burst pressure

	CAD width (μm)	CAD height (μm)	Measured width (μm)	Measured height (μm)	Aspect ratio (w/h)	Experimental burst pressure $P_{\text{b-exp}}$ (mbar)	Calculated burst pressure $P_{\text{b-the}}$ (mbar)	Measured contact angle (°)
Edge length (mm)				Reservoir footprint test (constant height 1.5 mm)				
3	70	100	97.51	63.49	1.54	16.4	16.42	116
2.5	70	100	83.1	71.2	1.17	16.1	16.46	116
2	70	100	96.4	62.4	1.54	16.9	16.66	116
1.5	70	100	84.21	61.63	1.37	16.9	17.74	116
1	70	100	100.38	63.82	1.57	18.9	16.18	116
0.5	70	100	76.38	59.19	1.29	10.8	11.90	106
0.4	70	100	76.46	59.69	1.28	11.5	11.84	106
0.3	70	100	88.64	59.46	1.49	11.7	11.15	106
0.2	70	100	94.18	58.1	1.62	11.3	11.04	106
Height (mm)				Reservoir height test (constant footprint 1.5 mm)				
1.5	80	100	107.96	58.82	1.84	19.8	18.91	120
1	80	100	110.73	60.42	1.83	18.4	18.42	120
0.5	80	100	91.35	62	1.47	19.6	19.49	120
0.25	80	100	119.03	58.79	2.02	17.9	18.3	120
Reservoir number				Consecutive reservoirs test				
1	80	60	83.98	50.36	1.67	12.8	11.07	104
2	80	60	81.77	49.64	1.65	12.2	11.28	104
3	80	60	111.6	41.9	2.66	18.2	11.44	104
4	80	60	87.29	50.9	1.71	15.4	10.84	104
5	80	60	75.14	51.03	1.47	16.6	11.46	104
6	80	60	78.45	50.37	1.56	15.2	11.36	104
7	80	60	110.5	46.28	2.39	17.4	10.68	104
8	80	60	88.4	49.39	1.79	15.7	10.99	104
9	80	60	80.66	49.19	1.64	15.6	11.4	104
10	80	60	80.66	50.51	1.60	15.9	11.22	104

Table 3 Measurement results and calculated burst pressure values of the channels that form the microfluidic chip with nine reservoirs arranged in three parallel chains

Channel	CAD width (μm)	CAD height (μm)	Measured width (μm)	Measured height (μm)	Calculated burst pressure $P_{\text{b-the}}$ (mbar)	Measured contact angle (°)
Inlet to 1	500	500	513.65	257.85	2.87	110
1 to 2–1	160	150	189.3	73.79	9.28	110
Inlet to 2–2	160	150	185.98	74.75	9.24	110
2–1 to 3–1	120	60	148.34	44.06	14.50	110
2–2 to 3–2	120	60	126.20	43.87	15.13	110
Inlet to 3–3	120	60	152.77	45.27	14.10	110
3–2 to 4–1	50	50	70.85	40.43	19.13	110
3–3 to 4–2	50	50	68.63	40.25	19.41	110
4–2 to 5	50	30	59.78	25.73	27.38	110
3–1 to outlet	40	30	52.03	17.5	37.61	110
4–1 to outlet	30	30	35.42	23.82	34.58	110
5 to outlet	40	30	40.96	27.06	30.22	110

power supply (Fig. S11). Later, the characterization on battery powered portable pressure pump was conducted. The pulse width modulation (PWM) value entered into the controller was increased in increments of 1, and the pressure from the pressure controller was adjusted accordingly. This adjustment continued until the oil level inside the microfluidic channel remained stationary (Fig. 5b), indicating that the pressure from our pump matched that from the controller.

2.6. LAMP assay on portable microfluidic system

The microfluidic chip shown in Fig. 6a, featuring two consecutive reservoirs in two parallel-connected lines, was engineered to conduct a LAMP-based point-of-care (PoC) detection assay. The reservoirs were designed to hold the liquid in the LAMP reservoirs for 30 minutes before pumping it to the imaging reservoirs. To serve as a control for detection, primers were lyophilized in only one of the two

This journal is © The Royal Society of Chemistry 2025

Open Access Article. Published on 04 August 2025. Downloaded on 6/16/2026 10:50:35 PM.
This article is licensed under a Creative Commons Attribution-NonCommercial 3.0 Unported Licence.

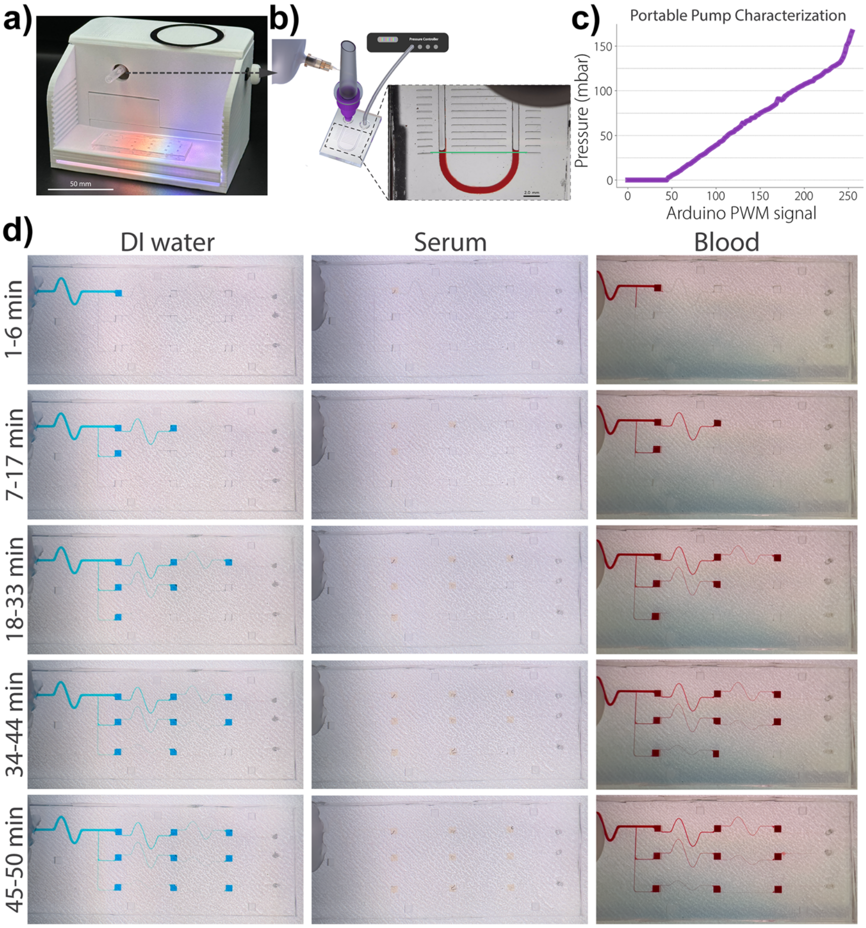

Fig. 5 Overview of the portable pressure pump, characterization setup, and performance testing with different fluids. (a) Photograph of the portable pressure pump. The built-in illumination displays rainbow colors when idle and switches to white light during the pumping cycle, which begins when the start button on the right side is pressed. Scale bar: 50 mm. (b) Illustration of the characterization setup: the liquid dispenser was placed at one end of the U-shaped channel after trapping the oil inside, while the other end was connected to the pressure controller. The U-shaped channel was filled with approximately 200 μL of lubrication oil, and the oil level was compared to structural horizontal lines on the microscope screen for measurement. Scale bar: 2 mm. (c) Pressure output characteristics of the portable pressure pump in response to signal values entered into the Arduino controller. (d) Testing 3 different fluids with the portable pump. Fluids were kept in reservoirs for specified time intervals.

parallel LAMP reservoirs. This approach allowed us to (1) determine whether the reaction products remained localized during the 30-minute incubation, and (2) more accurately quantify the resulting color changes in the primer-containing reservoir. The smartphone camera's field of view encompassed both sensing reservoirs, enabling simultaneous image capture and subsequent comparison of colorimetric intensity. The intensity in the sensing reservoir was measured and directly compared to the control (Fig. 7c and d). The details of the production of the chips is described in Fig. S5.

A module, incorporating a 15 × 15 mm Peltier element, was designed and integrated with the portable pressure pump (Fig. 6e). The Peltier device enabled temperature control at 65 °C for the LAMP reaction as detailed in section SI S8. To improve image quality, the readout regions were positioned over the back-illuminated white surface. Assembled LAMP chips were positioned on the heated side of the Peltier module (Fig. 6e), which was governed by an external DC controller.

The LAMP method is capable of rapidly amplifying the target gene region at constant temperature (isothermal conditions).[51,52] Plasmid DNAs encoding the target gene are commonly used in place of infectious virus isolates in the development, optimization, and validation of diagnostic devices and chip-based platforms.[53] Accordingly, a pUC57 plasmid construct encoding the Mpox-specific *F3L* gene—commonly targeted for specific detection of the virus—was generated and used as the template DNA in all off-chip and on-chip experiments.[54] The *F3L* gene sequence was retrieved from the reference genome of MPXV-Zaire-96-I-16 (NC_003310.1, GenBank: AF380138.1) available on the NCBI website. The assay was designed through the methods we described previously.[55] Briefly, LAMP reactions were performed using the WarmStart® Colorimetric LAMP 2X Master Mix (New England Biolabs, Ipswich, MA, USA) for

Open Access Article. Published on 04 August 2025. Downloaded on 6/16/2026 10:50:35 PM.
This article is licensed under a Creative Commons Attribution-NonCommercial 3.0 Unported Licence.

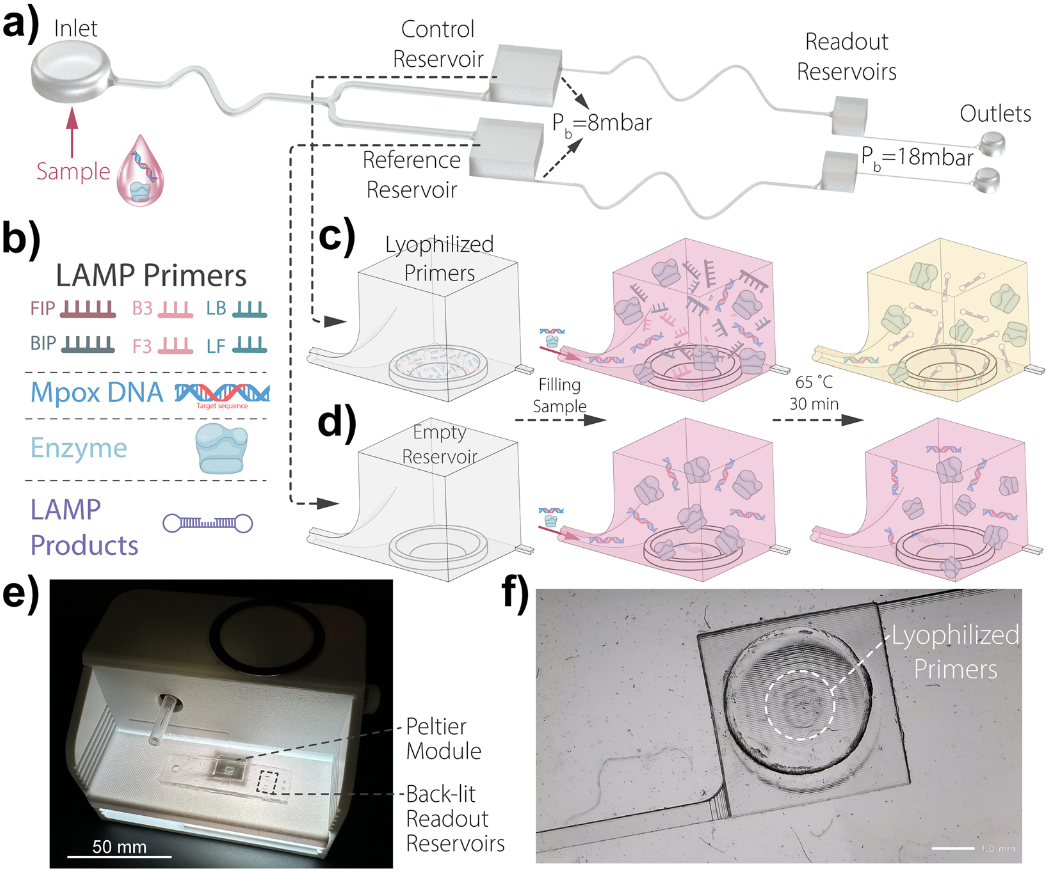

Fig. 6 Demonstration of the PoC LAMP system. (a) Microfluidic channel design for the LAMP-on-chip. The first two reservoirs are aligned with the heater in the pump and they are filled with sample simultaneously. The fluid stays there for 30 minutes while the temperature of the heater was adjusted to 65 °C. Next, the fluid is pumped to the following readout reservoirs, where the white light below enables capturing the color shift with smart phone camera. LAMP primers were immobilized only in one of the parallel reservoirs, providing comparison for changing color. (b) Illustrative list of the LAMP components. (c and d) Depiction of the procedure parallel reservoirs. The lyophilized primers (c) mix with the pumped sample (pink) while the other reservoir (d) only contains constituents of the sample. Following 30 minutes heat treatment, the LAMP reservoir's color change to yellow while the other remains pink. (e) The heating module on the portable pressure pump aligning the Peltier element with the reaction reservoir. The readout reservoirs are aligned with the backlit region, providing illumination for easy smart phone imaging. Scale bar 50 mm. (f) The microscope picture of the precipitated primers after lyophilization. Scale bar 1 mm.

visible colorimetric detection. The primer sets for amplifying the F3L gene were designed using the Primer Explorer V5 software (Eiken Chemical Co., Tokyo, Japan) and included six primers: FIP, BIP, F3, B3, LF, and LB. Primers were purchased from Sentebiolab (Turkey).

Initially, the functionality of the LAMP assay was assessed with off-chip reactions at 65 °C (SI section S5). The reaction mix consisted of 1 μL of pUC57 plasmid DNA (25 ng μL^{-1}), 12.5 μL of LAMP 2X master mix, 2.5 μL of primer mix and nuclease-free water to achieve a total reaction volume of 25 μL. Negative control was prepared without the DNA. Subsequently, a 10-fold serial dilution study starting from 100 ng μL^{-1} demonstrated that the LAMP assay maintained successful amplification down to a DNA concentration of 0.1 ng μL^{-1} (Fig. S6e). Off-chip reactions served both to ensure the proper performance of the LAMP assay and to validate the results of the on-chip, automated amplification process.

For on-chip reactions, a total of 6 μL of the primer mix with given concentrations was lyophilized into the LAMP reaction reservoir of the microfluidic chip (Fig. 6f). The volume of the LAMP reservoir is approximately 24 μL (4 × 4 × 1.5 mm). The primer mix was added excessively to compensate for potential losses during lyophilization. The sample was prepared by mixing 75 μL of colorimetric LAMP master mix, 6 μL of DNA, and 69 μL of water. Then the 150 μL mix was filled into a liquid dispenser and the test was conducted with the portable pressure pump. After performing successful on-chip amplification at a DNA concentration of 25 ng μL^{-1}, a 10-fold serial dilution study starting from 100 ng μL^{-1} was performed to evaluate the system's detection limitations (Fig. 7e and f).

The color shift to yellow due to LAMP was characterized by comparing the ratio of red to green (R/G) in smartphone captured images.[56] The red, blue, and green intensities of the reservoirs and their backgrounds were measured with ImageJ. Then all the channels were normalized by dividing with background values. The intensity of the blue channels were consistent while the red and green were shifting. The

Open Access Article. Published on 04 August 2025. Downloaded on 6/16/2026 10:50:35 PM.
This article is licensed under a Creative Commons Attribution-NonCommercial 3.0 Unported Licence.

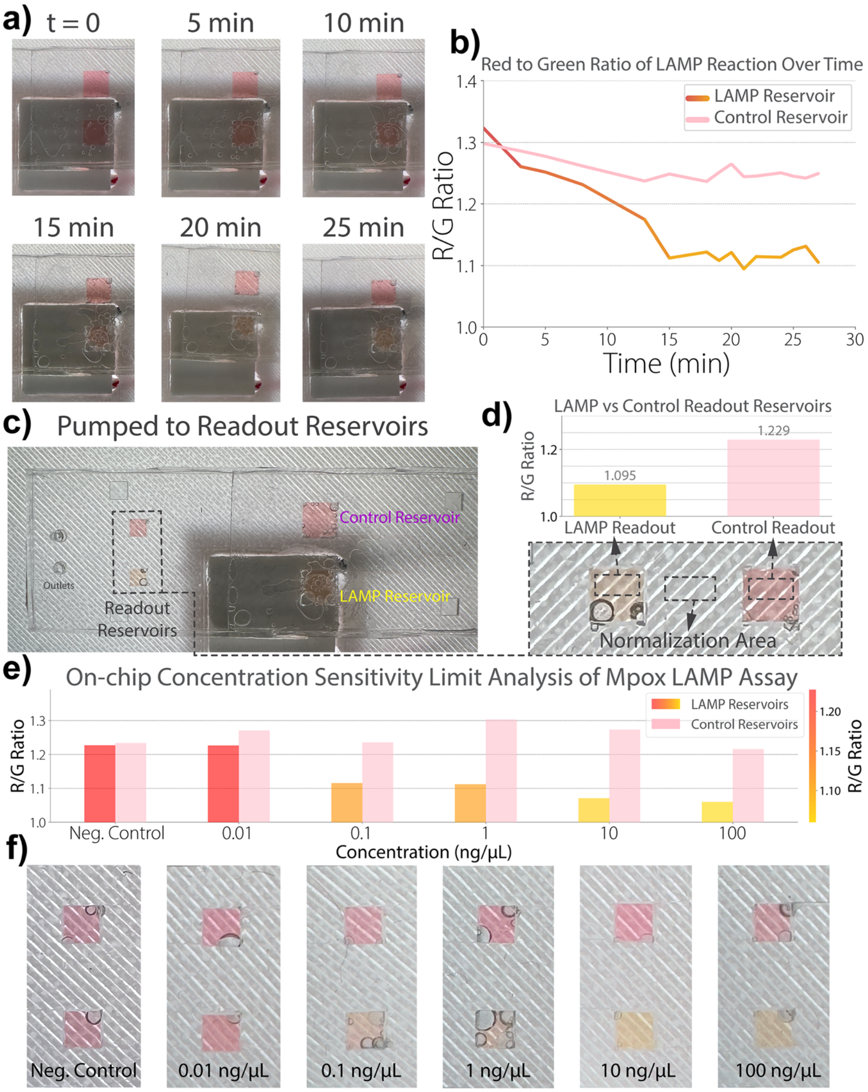

Fig. 7 Colorimetric LAMP on the microfluidic chip with the portable pressure pump. (a) Time-lapse images of the reservoirs during the reaction showing amplification dynamics for a 25 ng μL^{-1} plasmid DNA containing sample. The LAMP reservoir was aligned on the Peltier module for heating. (b) The change of red-to-green (R/G) ratio of liquids inside the reaction reservoirs. (c) Wider angle image showing that fluids were pumped to the following reservoirs after the reaction. The readout reservoirs are aligned with backlit region of the pump's heater slot. (d) Normalized R/G ratios of the readout reservoirs. Red, green, and blue intensities were normalized to a designated reference region on the chip to minimize variability caused by smartphone camera lighting. (e) On-chip sample concentration detection sensitivity study using four serial dilutions of Mpox specific gene cloned plasmid DNA (100 to 0.01 ng μL^{-1}). A visible color shift ($R/G < 1.15$) was observed down to 0.1 ng μL^{-1}. (f) Smartphone images of the readout reservoirs from the detection limit study. Lower reservoirs (LAMP) contain amplified reactions, while upper reservoirs (control) serve as references for comparison. The measurements of images correspond to the concentrations shown in (e).

color measurement method is detailed in SI section S6. Pictures presented in Fig. 7 are raw, unprocessed images taken with smartphone camera.

3. Results

3.1. Characterization of the reaction reservoirs

The characterization setup described in Fig. 2 enabled the determination of the burst pressure P_b with a tolerance of ±1 mbar. Fig. 3b shows that the contact angle significantly influences P_b. Individual measurement of the contact angle was crucial due to the complex nature of polydimethylsiloxane (PDMS) and rough structure of 3D printed molds (as detailed in the SI section S2). Therefore, we measured the contact angle before all experiments.

Since 3D printing can be inconsistent for dimensions below 150 μm, we measured the width and height of all printed channels to account for any variations. We assessed 19 designs with varying outlet channel widths (w) and heights (h) (Table 1). The effects of these dimensions on P_b were experimentally evaluated across these configurations, yielding experimental P_b values ranging from 6.4 to 44.8 mbar. Fig. 3a shows that the experimental results closely match the theoretical calculations, indicating the effectiveness of our

Open Access Article. Published on 04 August 2025. Downloaded on 6/16/2026 10:50:35 PM.
This article is licensed under a Creative Commons Attribution-NonCommercial 3.0 Unported Licence.

approach. Investigation of this dataset by comparing the difference between the experimental and theoretical P_b demonstrated that the equation reliably predicted P_b when the aspect ratio (w/h) was between 1 and 2 (Fig. 2c). Random deviations were observed at higher aspect ratios and we suspect that this may be due to inconsistency of surface contact angle through the channel caused by inhomogeneous penetration during the plasma treatment of high-aspect-ratio channels. Moreover, measured roughness of the molds correspond to the top and bottom walls of the channel. We were unable to measure the roughness of the side walls due to experimental limitations. Thorough experimentation of surface properties on side channels should be conducted for achieving better results with channels with aspect ratios greater than 2 and smaller than 0.5. Our manufacturing and characterization methods proved the eqn (1) is reliable for aspect ratios between 1 and 2. Building on these findings, we designed and manufactured precisely programmable reservoirs with burst pressures ranging from 2 to 35 mbar (Table 2). It should be emphasized that burst pressures above 35 mbar were measured; however, they were not reliably controllable due to dispersed aspect ratios. Consequently, we investigated additional parameters that might affect P_b.

Specifically, we examined the effects of the footprint and height of the reservoirs, which determine the reservoir volume—a critical factor in biological reactions. The impact of these parameters on P_b was tested in experiments depicted in Fig. 3d and e. To better understand their influence, we compared experimental P_b values to theoretical calculations based on measurements of channel widths, heights, and contact angles. Since the printed channels varied in dimensions, this comparative approach provided clearer insights into the phenomena. The results indicated that the effects of reservoir footprint and height on P_b were inconspicuous. Therefore, the reservoir volume can be designed according to the volume requirements of biological reactions without significantly affecting the burst pressure.

We also investigated whether hydrodynamic resistance affects the flow P_b in serially connected ten reservoirs (Fig. 3f). The outlets of all reservoirs were designed with the same cross-sectional dimensions, and their measured dimensions were consistent except for reservoirs 3 and 7 (Table 2). We observed higher P_b values for reservoirs following the first and second ones, indicating that hydrodynamic resistance influences P_b. However, the impact did not increase linearly with the number of reservoirs or the length of the channel. When the inlet pressure P_i was applied 0–4 mbar above of P_b, the fluid flowed through the channel at rates below 0.1 μL min^{-1}, corresponding to an approximate velocity of 0.4 mm s^{-1}. This results in a capillary number Ca $\ll$ 1, indicating a capillary-dominant system. Despite the observed effect on consecutive reservoirs, calculating this impact precisely requires further investigation. To eliminate possible flow blockages due to this unpredictability, we applied a P_i at least two times greater than P_b in the following experiments to ensure consistent fluid movement through the system. It should be noted that all experimental values except the contact angle effect measurements (Fig. 3b) were tested three separate times to create the dataset presented in the tables and figures, ensuring the reliability and reproducibility of our results. The P_b values were noted after confirming that the readouts from three measurements were in range of ±1 mbar.

3.2. Microfluidic chip with nine reservoirs arranged in three parallel chains

We engineered a microfluidic circuit incorporating both parallel and serially connected reservoirs (Fig. 1b). The dimensions of the connections between reservoirs were designed to direct fluid movement according to the scheme depicted in Fig. 1e. Measurement-based calculations of the P_bs for the outlets of these reservoirs are provided in Table 3. The system performed as expected when operated with the Python script controlling the pressure controller. Fig. 4a presents the real-time recorded P_i and the flow rate measured at the inlet. The flow rate exhibits a peak at the onset of each process step and then reduces to zero during the waiting period of each of the five steps. The images in Fig. 4 were captured during the indicated time intervals. It should be noted that the chip was connected to the setup described in Fig. 2b, and the process was recorded without any intervention. The real-time video recording of the chip and associated data are available in the Video S1.

This experiment demonstrates that the 3D-printed reservoirs can support consecutive and parallel reactions relying solely on automated pressure inputs. The system was designed in accordance with eqn (1), and the automated manipulation was achieved using a script based on this design. The script is available on our lab page and can be edited to set the waiting time in each reservoir to application-specific values.

The sinusoidal pathways between reservoirs facilitate micromixing of transported species and help mitigate effects of possible pressure bursts during the procedure by preventing direct flow into the subsequent reservoir. However, the printer's resolution limited the fabrication of sinusoidal paths in channels with widths less than 60 μm. Consequently, the channels from reservoir 3–2 to 4–1, from 3–3 to 4–2, and from 4–2 to 5 were designed to be more linear.

The flow rate fluctuations observed around zero during the waiting times were a result of the pressure controller's instability in systems with outlets exposed to uncontrolled pressure (atmospheric pressure). As can be observed in the Video S1, this behavior did not adversely affect the retention of fluid within the reservoirs. On the contrary, we believe that these fluctuations may enhance the efficiency of reactions by promoting increased convection and mixing inside the reservoirs.

Predicting fluid behavior in parallel configurations is more challenging. The total resistance to flow increases

Open Access Article. Published on 04 August 2025. Downloaded on 6/16/2026 10:50:35 PM.
This article is licensed under a Creative Commons Attribution-NonCommercial 3.0 Unported Licence.

proportionally with the number of parallel branches in the system. Additionally, the overall flow rate into the system increases, leading to a higher *Ca*. We addressed this issue by applying a pressure significantly higher than P_b at the beginning and gradually decreasing it to a value below P_b. This strategy facilitated rapid transport to subsequent reservoirs—in under a minute. Moreover, this transport time can be easily tuned for specific reactions by adjusting the inlet pressure. If the applied pressure remains slightly above the burst pressure, the fluid delivery occurs over longer durations, especially in parallel channel configurations.

To conclude, multiple reservoirs can be adapted to various methods of automated fluid transport, significantly enhancing the flexibility of microfluidic systems. For instance, designing a reservoir with multiple outlets, each having different P_b values, allows the same fluid to be sequentially directed to different reaction pathways at predetermined times. Such a chip could sequentially supply a reagent to four different detection zones, each activating at specific pressures and times. This adaptability is particularly useful in multiplexed assays, where simultaneous or sequential analysis of multiple targets is required. By customizing the P_b values and channel designs, our microfluidic platform can accommodate a wide range of biochemical assays and diagnostic applications, enhancing its versatility and utility in point-of-care testing and other analytical fields.

3.3. Portable pressure pump

We developed a portable pressure pump capable of supplying pressures ranging from 2.8 to 166 mbar to microfluidic channels, realized at a cost of $62.6. Our primary objective was to enable point-of-care (PoC) applications of microfluidic circuits with bio-reaction reservoirs, and the pump effectively served this purpose. The leaking structure of the 3D-printed air tank played a crucial role in providing stable pressure below 200 mbar. While the commercial air pump used has a minimum pressure output above 1 bar and exhibits pulsatile behavior, the intentional air leaks along the connection—from the air tank through the needle and liquid dispenser (Fig. 1d) — facilitated both stabilization and reduction of pressure.

As demonstrated in Fig. 5c, the system's pressure output was consistent with that supplied by the Elveflow pressure controller, which fluctuates within ±1 mbar of target values. We utilized an Arduino microcontroller and an 11.1 V battery (12.6 V when fully charged) to operate the system. This setup was able to supply a maximum of 11.78 V to the air pump, corresponding to a maximum applied pressure of 166 mbar.

The body of the pump was designed to facilitate the easy adaptation of different modules. We integrated a heating module for the application of the LAMP assay. Additional modules for cooling, lighting, and sensing can be easily integrated by 3D-printing components compatible with the mounting slots. For applications requiring advanced computing capabilities, such as optical sensing, more powerful controllers than the Arduino may be utilized.

All software and the CAD models used in the device are available on our lab repository, aiming to provide users with an affordable pump, which can be customized to their specific needs by integrating distinct modules.

3.4. Precise manipulation of body liquids with portable pressure pump

We successfully automated the pumping of deionized (DI) water, blood and serum through the complex microfluidic chip described in section 2.4 using our portable pressure pump. The reservoirs' rest durations were set to 5, 10, 15, 10, and 5 minutes at reservoir steps 1, 2, 3, 4, and 5, respectively. Unlike the experiments conducted with the advanced pressure controller, we used a different recipe, demonstrating that fluid stay times in parallel-arranged reservoirs can be tuned solely by adjusting the inlet pressure. We kept the transfer time between consecutive reservoirs under one minute by briefly applying a pressure considerably higher than the burst pressures of the reservoirs.

Notably, the diffusion of lyophilized material into the liquid depends on both the lyophilized volume and the reservoir volume. In an experiment where food coloring was dried in a reservoir, the color dispersed homogeneously within about 5 minutes (Fig. S4). Consequently, we recommend allowing at least five minutes of rest to ensure thorough dissolution. Nonetheless, we did not observe any upper limit on the resting duration for water-based liquids, allowing the user to extend it as needed for any given reaction. However, when working with fluids prone to viscosity changes or precipitation—such as blood or other complex biological samples—additional precautions are necessary to prevent clogging in the narrow reservoir outlets.

Since fluids like saliva, urine, fetal bovine serum (FBS), Dulbecco's modified Eagle medium (DMEM), and bovine serum albumin (BSA) are water-based solutions, the automated control with DI water validates that the reservoirs are suitable for procedures involving these fluids. The pressure script used with the Elveflow pressure controller was converted into an Arduino script based on the characterization shown in Fig. 5c. Our portable pump successfully delivered the water at the desired times, replicating the performance achieved with the pressure controller (Fig. 5d).

The contact angles for blood and serum was measured separately. In these experiments, the portable pump was controlled manually through GUI. Blood and serum are the most information-rich bodily fluids related to diseases,[57] and we demonstrated that these fluids can be manipulated in the system using our pressure pump. Notably, the contact angle of serum on PDMS was slightly above 90°, prompting us to maintain minimal inlet pressure during the waiting steps to accommodate low burst pressures. Under these conditions, serum flowed smoothly through the system, confirming the

Open Access Article. Published on 04 August 2025. Downloaded on 6/16/2026 10:50:35 PM.
This article is licensed under a Creative Commons Attribution-NonCommercial 3.0 Unported Licence.

robustness of our approach for handling it in point-of-care settings.

Blood's contact angle on PDMS was measured to be 108 degrees, confirming that the use of reservoirs is feasible. However, clogging was observed in the narrow channels during the wait steps, likely due to a slight temperature increase on the chip caused by the pump's LED illumination. Specifically, the outlet channels of reservoirs 3–1, 3–2, and 3–3 clogged when operated without cooling (Fig. S15). To overcome this issue, ice was placed between the holding module and LEDs. The system functioned as designed except for the last step with cooling, which is pumping the fluid out of all channels. These findings showed us that the reservoirs with outlet channels dimensioned above 100 microns can be used at room temperature in blood based assays, while smaller channels necessitate proper temperature control. In conclusion, the reservoirs' and the pump's effectiveness for bioassays was demonstrated.

3.5. PoC detection of Mpox with colorimetric LAMP-on-chip

The visible colorimetric detection is based on color changes resulting from pH changes associated with the LAMP reaction.[51] As illustrated in Fig. 6c and d, the pH change causes a color change from pink to yellow. Consequently, pink indicates no amplification and a negative result, while yellow indicates the presence of amplification and a positive result. As demonstrated in Fig. S6, the off-chip experimentation of the assay showed that after 30 minutes of incubation at 65 °C, the control tube appeared pink to the naked eye. In contrast, the test sample containing pUC57 plasmid DNA turned yellow, indicating a positive result.

Following the validation of the assay, the LAMP-on-Chip was first performed using a 25 ng μL^{-1} Mpox plasmid DNA containing sample. The reservoir volume was 24 μL which closely matched the 25 μL off-chip reactions (SI section S5). The microfluidic chip shown in Fig. 6a served fluid manipulation as expected in room temperature (Table 4). The LAMP reaction requires a temperature of 65 °C and it was achieved with the integrated Peltier element. Rather than employing real-time temperature control, our heating system relied on pre-calibrated voltage values (SI section S8). Since LAMP reaction requires precise isothermal conditions, its successful execution confirms the effectiveness of our heating setup.

Additionally, the Peltier element enabled local heating of the reaction reservoirs, which is crucial for enabling controlled thermal conditions. Heating the inlet channels of the microfluidic chip can cause considerable problems related to flow control, such as uncontrollable bubble formation. The small Peltier element addressed this need adequately but was energy-intensive, particularly for isothermal reactions like LAMP. Thus, it was not possible to heat with the included pump battery. Small, localized resistive heaters might be a more effective approach to this purpose. Such systems also enable built-in feed-back mechanisms for improved heat control.[58] Further confining the heating to only the reaction reservoirs would significantly help the management of bubble formation. Nevertheless, the Peltier element remains a valuable option for processes requiring cyclic heating and cooling. Additionally, integrated pump modules that enclose the chip could enhance thermal stability for reactions requiring precise temperature control. While we did not observe any environmental interference in our setup, such enclosures may be necessary for certain applications where external temperature fluctuations could affect reaction performance.

The control of evaporation of the sample fluid during the reaction is one of the most challenging parts of microfluidic reactions that require heat treatment. The negative effects of this phenomenon is mostly limited by sealing the fluid from contacting the air by inlet lids or enclosing chips with a tape.[28,33] Yet, our pumps design works on the air pressure that is applied to the channel. This limited the application of such enclosures. To reduce the amount of permeation through the PDMS above the reaction reservoirs, we included a transparent tape that covers this area (Fig. S5). Experiment was started by pumping the sample into reservoirs at room temperature. Then the heater was turned on to initiate the reaction in the LAMP reservoir. The bubbles started forming inside the chamber. The inlet pressure was kept around 3 mbar during the reaction and this helped compensate for the fluid that is lost due to evaporation. The entrapment of created bubbles inside the reservoirs created undesired pressure fluctuations, causing small volumes of fluid to escape out of the reservoir. Still, the volume of this portion did not affect the reaction. The consistent pressure application on the inlet also restored this portion, keeping the reaction volume stable and reaction continuous.

Time-lapse images of the process (Fig. 7a) and color intensity measurements from bubble-free regions showed a noticeable R/G ratio change in the LAMP reservoir. However, bubble formation within the reaction reservoirs reduced image quality, making precise quantification more

Table 4 Measurement based calculation of burst pressure of reservoirs of LAMP chip

Channel	Measured width (μm)	Measured height (μm)	Measured contact angle (°)	Calculated burst pressure $P_{\text{b–the}}$ (mbar)
Inlet to LAMP reservoir	201.1	223.6	108	4.20
Inlet to control reservoir	195.58	224	108	4.26
Lamp R. to readout	156.91	79.3	108	8.45
Control R. to readout	185.64	78.25	108	8.08
LAMP readout to outlet	64.09	36.57	108	19.11
Control readout to outlet	66.3	38.79	108	18.18

Open Access Article. Published on 04 August 2025. Downloaded on 6/16/2026 10:50:35 PM.
This article is licensed under a Creative Commons Attribution-NonCommercial 3.0 Unported Licence.

challenging. Additionally, the Peltier module blocked backlighting, further reducing visibility. Despite these issues, normalization of reservoir images relative to their own backgrounds (SI section S6) enabled relative measurement of the color shift (Fig. 7b). Although the reaction time was set to 30 minutes, time-lapse analysis revealed that the yellow color shift became visibly distinguishable to the naked eye after approximately 20 minutes. This suggests that colorimetric detection can be achieved without instrumentation within this timeframe. Furthermore, quantitative analysis of R/G values indicated that the color shift continued for 15 minutes, reaching an R/G ratio of approximately 1.1. Small fluctuations in measured values beyond this point were likely influenced by minor variations in our imaging and quantification method, rather than a continuation of the reaction itself. Based on these observations, we report 20 minutes as the reliable distinguishable readout time for this sample concentration (25 ng μL^{-1}), corresponding to the moment when the yellow color shift becomes stable and differentiable from the control.

After the reaction time was completed, the heater was turned off and waited for stabilization to room temperature. Then the fluids were pumped to following readout reservoirs by increasing the inlet pressure (Fig. 7c). Successful operation of this step proved that the reservoirs can be used for automation of consecutive reactions. The amount of bubbles transferred from reaction reservoirs to the readout reservoirs were limited. Notably, if the transfer between reservoirs is conducted while the system is still hot, more bubbles form in the readout reservoirs. The inlet fluid from the liquid dispenser was still purple since the reaction only occurred in the LAMP reservoir. The fluid transported from this reservoir to following reservoir was noticeably yellow to naked eye, proving that mostly the products of the reaction were transferred. This proves the suitability of the automated reaction reservoirs for sequential reactions.

As shown in Fig. 7d, color intensity measurements of smartphone images of the readout reservoirs allowed us to quantify the R/G ratio difference between the control and LAMP reservoirs, which were 1.23 and 1.09, respectively. However, on-chip assays are inherently more vulnerable to evaporation due to the elevated reaction temperature. This evaporation can significantly alter reaction conditions, particularly at lower DNA concentrations, where minor volume losses can lead to reduced amplification efficiency and less pronounced colorimetric changes. Additionally, smartphone cameras introduce variability in image capture—due to automatic lighting adjustments and lens limitations—making them less ideal for consistent quantitative analysis. The detection capabilities of the system was further tested through a detection sensitivity study.

3.6. Sensitivity analysis of the on-chip LAMP system

An off-chip 10-fold serial dilution experiment revealed that the assay could reliably detect plasmid DNA at concentrations as low as 0.1 ng μL^{-1} (Fig. S6). Despite the technical limitations discussed in the previous section—such as evaporation effects and smartphone-based imaging variability—the same dilution series was successfully performed on-chip, achieving comparable sensitivity levels (Fig. 7e and f). Time-lapse analysis of color development during the serial dilution experiments revealed that color changes occurred more rapidly at higher DNA concentrations—approximately 10 minutes for 100 ng μL^{-1} and 15 minutes for 10 ng μL^{-1} (Fig. S7). In contrast, reactions containing 1 ng μL^{-1} and 0.1 ng μL^{-1} required at least 25 minutes to exhibit a significant color shift, confirming that the full 30-minute incubation period is critical for detecting lower DNA concentrations.

To evaluate whether the observed color changes were a result of true amplification or heat or bubble-induced artifacts, we conducted an on-chip negative control study using a reaction mixture without plasmid DNA (Fig. S8). During the heating process, both the LAMP and no-primer control reservoirs exhibited transient decreases in R/G values to approximately 1.2—similar to values observed in the early stages of positive amplification. However, these shifts were reversible, with R/G ratios returning to baseline upon cooling. Notably, despite the temporary drop in measured values, the reaction mixtures retained a pink appearance to the naked eye throughout the experiment. These findings confirm that elevated temperature can induce false-positive signals in quantitative continuous image analysis.

Thus, while reaction reservoirs are valuable for comparing reaction timing across different concentrations, they are not reliable indicators of true amplification and should not be used as the primary detection readout. Instead, detection should be based on the cooled fluid transferred to downstream readout reservoirs. In true positive samples, amplification results in a stable yellow shift that persists at room temperature, whereas thermal and bubble related artifacts disappear upon cooling. In our experiments, the reliability of real-time, quantifiable detection was primarily limited by bubble formation within the reaction reservoir. To preserve the automation and accessibility of fluid handling, we did not introduce full physical enclosures around the chip during testing. Incorporating such enclosures may enhance the stability and accuracy of real-time optical detection, which should be considered in future system designs.

Accordingly, the final determination of the on-chip detection limit was based on measurements in the readout reservoirs (Fig. 7f). DNA concentrations ≥0.1 ng μL^{-1} produced visually distinguishable yellow coloration with R/G ratios below 1.15. The 0.01 ng μL^{-1} sample showed only a minor decrease in R/G ratio and remained predominantly pink (R/G $>$ 1.2), indicating no reliable detection at this concentration. Although comparative analysis of reaction reservoirs (Fig. S7e) revealed subtle color changes in the 0.01 ng μL^{-1} sample, the corresponding behavior in the negative control (Fig. S8b) confirmed these shifts were heat-induced rather than indicative of amplification.

Open Access Article. Published on 04 August 2025. Downloaded on 6/16/2026 10:50:35 PM. This article is licensed under a Creative Commons Attribution-NonCommercial 3.0 Unported Licence.

In conclusion, the portable on-chip system successfully demonstrated sensitive operation and measurement of Mpox LAMP assay. Notably, the on-chip experiments produced comparable visual and optical readouts to off-chip experiments across the same concentration range, confirming that the platform effectively mobilizes and automates the LAMP assay for disease detection. Based on the sensitivity threshold of 0.1 ng μL^{-1}, the limit of detection (LoD) was determined to be 2.76×10^7 copies per μL (SI section S5). Future enhancements to sensitivity may include the integration of higher-resolution cameras or dedicated optical sensors into the modular pump system. Additionally, adopting fluorometric detection—using fluorescent dyes and excitation sources—could offer more precise, quantitative readouts and reduce dependence on ambient lighting and smartphone-based imaging.

Discussion

Hydrophobic valve-based microfluidic systems have been previously explored for fluid control in biological assays. Passive hydrophobic valves with channel dimensions of 100 μm in width and 40 μm in height have been successfully used for the parallel distribution of fluids into microchambers.[15] More recently, Chang *et al.* developed a highly integrated system incorporating multiple hydrophobic valve-integrated reaction chambers arranged in parallel, with channel dimensions as small as 380 μm in width and 17 μm in height.[33] This approach enabled multiplexed bio-assays within a compact, pipette-regulated microfluidic platform. Additionally, hydrophobic valves have been integrated with centrifugal microfluidics, where fluid flow is regulated based on rotational speed, allowing timing-dependent activation of reaction chambers.[59,60] Nonetheless, none of these approaches provide the high-precision flow control and programmability that pressure-driven systems offer.

In this study, we developed pressure-controlled, hydrophobic valve-based programmable bio-reaction reservoirs that enables precise flow regulation in both serial and parallel configurations. We first demonstrated the feasibility of using 3D-printed soft lithography to fabricate hydrophobic microfluidic channels with dimensions as small as 28 μm in width or 21 μm in height. While 3D printing offers versatility and cost efficiency for creating complex circuits with the proposed reaction reservoirs, dimensional inconsistencies were observed in channels narrower than 100 μm, posing a challenge for precise fabrication. To address this issue, we employed a measurement-based approach to achieve more accurate calculations of the burst pressure, enhancing the reliability of our microfluidic devices.

Our findings showed that reservoir outlets with low aspect ratios can effectively automate fluid flow within microfluidic systems by precisely tuning burst pressures up to 35 mbar. The chip shown in Fig. 3f demonstrated that fluid could be controlled across 10 consecutive reservoirs through regulation of only inlet pressure, without requiring additional valving mechanisms. This validates the system's ability to autonomously execute serial reactions, an essential feature for applications requiring multi-step bio-reaction sequences. Furthermore, the nine-reservoir chip, arranged in three parallel chains, operated precisely as designed, highlighting the versatility and programmability of the approach. The ability to control both subsequent and simultaneous reactions within a single microfluidic platform expands the potential for complex high-throughput biological workflows. Yet, the flow dynamics between complex sequential steps were approximated by applying instantaneous greater inlet pressures than the burst pressures of reservoirs, emphasizing the need for further investigation into the fluid mechanics of systems with parallel-connected reservoirs. Simulation of these intricate two-phase flows is computationally intensive and not practical. Despite these challenges, our experimental results confirm that pressure-controlled microfluidic reservoirs can be created and operated through automation for various biological reactions.

The portable pressure pump we developed successfully replicated the functionality of expensive and bulky commercial pumps, providing a low-cost, compact alternative well-suited for point-of-care applications. Its adaptable structure readily accommodates the addition of new modules; for instance, we integrated a heating module that facilitated LAMP. However, the current design operates on an open-loop system without real-time feedback, which restricts precise pressure control under varying experimental conditions. Future enhancements could include integrating a real-time pressure sensor into the air tank for closed-loop control. Similarly, adding a temperature sensor module would enable more precise thermal cycling during reactions. A noted limitation is that the pump currently functions only with microfluidic chips featuring a single inlet. Nevertheless, given the cost-efficiency of the air pump and the 3D-printed air tank, this system can be modified to support chips with multiple inlets, expanding its versatility. To support broader adoption and customization, we have made all of the pump's design files publicly available, enabling other researchers to integrate and build upon the system. Our results demonstrate that the pump effectively facilitates point-of-care applications of microfluidic systems relying on inlet pressure manipulation.

The lyophilization of LAMP primers within the reservoirs enabled the creation of an automated, portable disease-detection kit, highlighting the practical potential of our bio-reaction system for diagnostic applications. Critically, the production scheme we developed offers a robust, straightforward method for immobilizing biological agents into microfluidic structures: it is fully compatible with established soft lithography protocols, works seamlessly with plasma bonding, and does not require additional materials or processes for device assembly. One key challenge in implementing on-chip LAMP was addressing evaporation and bubble formation at elevated temperatures. However, we mitigated these issues without resorting to external

Open Access Article. Published on 04 August 2025. Downloaded on 6/16/2026 10:50:35 PM.
This article is licensed under a Creative Commons Attribution-NonCommercial 3.0 Unported Licence.

enclosures or humidity controls, thereby confirming that the reservoir design effectively limits evaporation during the reaction. Notably, our system's successful operation at 65 °C highlights the significance of the lyophilization-based manufacturing scheme, as most biological assays require temperatures below this threshold. Collectively, these findings demonstrate that our reservoirs can reliably support a variety of biochemical reactions, marking a substantial advancement in the development of integrated, on-chip diagnostic devices.

The integration of the portable pump, modular bioreaction reservoirs, and a smartphone allowed us to develop a remote, on-chip platform for application of a colorimetric Mpox LAMP assay. Using smartphone-based image analysis, we confirmed that the colorimetric shift associated with LAMP amplification could be reliably detected. However, the system's current LoD was primarily constrained by the limited sensitivity and variability of smartphone camera. Incorporating specialized cameras or more sensitive optical systems into the modular pressure pump could substantially improve detection sensitivity in future iterations. Despite this limitation, our device's liquid handling automation proved exceptionally robust. By simply adjusting the inlet pressure—which can be remotely automated *via* scripting—we could dispense the sample from a low-cost, commercially available tube, maintain it in the reaction reservoir for the required incubation period, and then transfer the reaction products sequentially into readout reservoirs. Although our current platform does not provide a dedicated sample preparation module, the high level of automation it offers could readily accommodate upstream processes, such as adding lysis agents, to enable remote sample preparation as well. This level of fluidic control offers strong potential for multi-step assays. For instance, an upstream reservoir containing lysis agents could lyse patient samples; the lysed biomarkers could then be routed through channels engineered to separate desired particles, and finally transferred to a reservoir holding amplification primers (*e.g.*, LAMP or PCR). Subsequent reservoirs may be coupled with advanced biosensors, facilitating a more sensitive, high-performance diagnostic workflow. Overall, our microfluidic platform holds a significant promise for advancing point-of-care diagnostics and facilitating a wide range of biochemical assays.

Conclusion

Here, we conducted a detailed three-dimensional experimental characterization of hydrophobic valves within microfluidic systems. Our findings demonstrated that reservoirs utilizing this phenomenon effectively enable automated flow control when coupled with the low-cost, portable pressure pump we developed. The modularity and versatility of our system were validated through the successful detection of Monkeypox disease markers using colorimetric loop-mediated isothermal amplification (LAMP) assay on a chip. These results underscore our goal of showing that complex microfluidic systems can be created for bioassays with various fluids at the point of care, advancing the accessibility and efficiency of diagnostic technologies.

Author contributions

Conceptualization – Mehmet Tugrul Birtek, Nazente Atceken, Savas Tasoglu. Data curation – Mehmet Tugrul Birtek, Nazente Atceken. Formal analysis – Mehmet Tugrul Birtek, Nazente Atceken. Funding acquisition – Savas Tasoglu. Investigation – Mehmet Tugrul Birtek, Nazente Atceken. Methodology – Mehmet Tugrul Birtek, Nazente Atceken. Project administration – Savas Tasoglu. Resources – Savas Tasoglu. Software – Mehmet Tugrul Birtek. Supervision – Savas Tasoglu. Validation – Mehmet Tugrul Birtek, Nazente Atceken. Visualization – Mehmet Tugrul Birtek. Writing – original draft – Mehmet Tugrul Birtek, Nazente Atceken. Writing – review & editing – Savas Tasoglu.

Conflicts of interest

The authors declare that there is no conflict of interest.

Data availability

Supplementary information is available. The PDF contains manufacturing and testing details of reaction reservoirs, portable pressure pump, and the LAMP assay. Supplementary Video 1: The experimental video of the microfluidic chip with nine reservoirs arranged in three parallel chains, controlled with Elveflow pressure controller. The Python script used during this experiment is available in our lab repository. Recording and data collection was started simultaneously. Video is speeded up at the ratios shown on the right of the time indicator. Measured pressure and flow rate values shown below are recorded simultaneously with the recording. Supplementary Video 2: The operation of the portable pressure pump. In pre-scribed pressure cycle mode, the pumping starts after 3 blinks of rainbow colors upon pressing the start button. The illumination remains white during experiments. See DOI: **https://doi.org/10.1039/D5LC00003C**

Codes and 3D printable files used in this study are open to access in our lab repository at **https://dxbiotech.ku.edu.tr/**.

Acknowledgements

Authors thank Ece Ozturk for providing access to the lyophilization device and Sevgi Sarica for the operation of the device. In addition, we thank Selim Olcer for assistance while producing the portable pressure pump. We also thank Ali Norouzi for their help in surface roughness measurements. ST acknowledges Tubitak 2232 International Fellowship for Outstanding Researchers Award (118C391), Alexander von Humboldt Research Fellowship for Experienced Researchers, Marie Skłodowska-Curie Individual Fellowship (101003361), and Royal Academy Newton-Katip Çelebi Transforming Systems Through Partnership Award (120 N019) for financial

Open Access Article. Published on 04 August 2025. Downloaded on 6/16/2026 10:50:35 PM.
This article is licensed under a Creative Commons Attribution-NonCommercial 3.0 Unported Licence.

support of this research. In addition, NA and ST acknowledge financial support from TÜBİTAK-2218 Domestic Postdoctoral Research Scholarship Project (122C195) and TÜBİTAK-1001 Scientific and Technological Research Project (123S582). The authors have no other relevant affiliations or financial involvement with any organization or entity with a financial interest in or financial conflict with the subject matter or materials discussed in the manuscript apart from those disclosed.

References

1 G. Chen, *et al.*, Electronic Textiles for Wearable Point-of-Care Systems, *Chem. Rev.*, 2022, **122**(3), 3259–3291.

2 S. K. Sia and L. J. Kricka, Microfluidics and point-of-care testing, *Lab Chip*, 2008, **8**(12), 1982–1983.

3 C. M. Pandey, *et al.*, Microfluidics Based Point-of-Care Diagnostics, *Biotechnol. J.*, 2018, **13**(1), 1700047.

4 A. K. Yetisen, M. S. Akram and C. R. Lowe, Paper-based microfluidic point-of-care diagnostic devices, *Lab Chip*, 2013, **13**(12), 2210–2251.

5 S. Battat, D. A. Weitz and G. M. Whitesides, An outlook on microfluidics: the promise and the challenge, *Lab Chip*, 2022, **22**(3), 530–536.

6 L. Y. Yeo, *et al.*, Microfluidic devices for bioapplications, *Small*, 2011, **7**(1), 12–48.

7 J. M. Ayuso, *et al.*, A role for microfluidic systems in precision medicine, *Nat. Commun.*, 2022, **13**(1), 3086.

8 J. Ko, *et al.*, Microfluidic high-throughput 3D cell culture, *Nat. Rev. Bioeng.*, 2024, **2**(6), 453–469.

9 J. Zhai, *et al.*, Drug screening on digital microfluidics for cancer precision medicine, *Nat. Commun.*, 2024, **15**(1), 4363.

10 X. Xu, *et al.*, Microfluidic Single-Cell Omics Analysis, *Small*, 2020, **16**(9), e1903905.

11 J. Atencia and D. J. Beebe, Controlled microfluidic interfaces, *Nature*, 2005, **437**(7059), 648–655.

12 A. J. DeMello, Control and detection of chemical reactions in microfluidic systems, *Nature*, 2006, **442**(7101), 394–402.

13 B. Mosadegh, *et al.*, Next-generation integrated microfluidic circuits, *Lab Chip*, 2011, **11**(17), 2813–2818.

14 S. J. Kim, *et al.*, Microfluidic automation using elastomeric valves and droplets: reducing reliance on external controllers, *Small*, 2012, **8**(19), 2925–2934.

15 D. Natsuhara, *et al.*, A Microfluidic Diagnostic Device Capable of Autonomous Sample Mixing and Dispensing for the Simultaneous Genetic Detection of Multiple Plant Viruses, *Micromachines*, 2020, **11**(6), 540.

16 D. Zaremba, S. Blonski and P. M. Korczyk, Integration of capillary-hydrodynamic logic circuitries for built-in control over multiple droplets in microfluidic networks, *Lab Chip*, 2021, **21**(9), 1771–1778.

17 W. Lee, *et al.*, Programmable DNA-Based Boolean Logic Microfluidic Processing Unit, *ACS Nano*, 2021, **15**(7), 11644–11654.

18 A. Shebindu, *et al.*, A programmable microfluidic platform to monitor calcium dynamics in microglia during inflammation, *Microsyst. Nanoeng.*, 2024, **10**(1), 106.

19 A. Beck, *et al.*, Logic Circuits Based on Chemical Volume Phase Transition Transistors for Planar Microfluidics and Lab-on-a-Chip Automation, *Adv. Mater. Technol.*, 2022, **7**(11), 2200185.

20 H. Gong, A. T. Woolley and G. P. Nordin, High density 3D printed microfluidic valves, pumps, and multiplexers, *Lab Chip*, 2016, **16**(13), 2450–2458.

21 R. Amin, *et al.*, 3D-printed microfluidic devices, *Biofabrication*, 2016, **8**(2), 022001.

22 M. A. Unger, *et al.*, Monolithic Microfabricated Valves and Pumps by Multilayer Soft Lithography, *Science*, 2000, **288**(5463), 113–116.

23 J. A. Weaver, *et al.*, Static control logic for microfluidic devices using pressure-gain valves, *Nat. Phys.*, 2010, **6**(3), 218–223.

24 Y. S. Lee, N. Bhattacharjee and A. Folch, 3D-printed Quake-style microvalves and micropumps, *Lab Chip*, 2018, **18**(8), 1207–1214.

25 K. A. Gopinathan, *et al.*, A microfluidic transistor for automatic control of liquids, *Nature*, 2023, **622**(7984), 735–741.

26 S. Wang, *et al.*, A Review of Capillary Pressure Control Valves in Microfluidics, *Biosensors*, 2021, **11**(10), 405.

27 M. Xie, *et al.*, Programmable Microfluidics Enabled by 3D Printed Bionic Janus Porous Matrics for Microfluidic Logic Chips, *Small*, 2023, **19**(34), e2300047.

28 D. Natsuhara, *et al.*, A microfluidic diagnostic device with air plug-in valves for the simultaneous genetic detection of various food allergens, *Sci. Rep.*, 2022, **12**(1), 12852.

29 Y. Y. Feng, *et al.*, Passive valves based on hydrophobic microfluidics, *Sens. Actuators, A*, 2003, **108**(1–3), 138–143.

30 S. Razavi Bazaz, *et al.*, 3D Printing of Inertial Microfluidic Devices, *Sci. Rep.*, 2020, **10**(1), 5929.

31 S. Lee, *et al.*, PDMS micro check valve with 3D valve disk for reducing fluid resistance, *J. Micromech. Microeng.*, 2024, **34**(8), 5009.

32 D. Najjar, *et al.*, A lab-on-a-chip for the concurrent electrochemical detection of SARS-CoV-2 RNA and anti-SARS-CoV-2 antibodies in saliva and plasma, *Nat. Biomed. Eng.*, 2022, **6**(8), 968–978.

33 Y. W. Chang, *et al.*, Pipette-operable microfluidic devices with hydrophobic valves in sequential dispensing with various liquid samples: multiplex disease assay by RT-LAMP, *Lab Chip*, 2024, **24**(12), 3112–3124.

34 A. P. Iakovlev, A. S. Erofeev and P. V. Gorelkin, Novel Pumping Methods for Microfluidic Devices: A Comprehensive Review, *Biosensors*, 2022, **12**(11), 956.

35 J. Park and J. K. Park, Integrated microfluidic pumps and valves operated by finger actuation, *Lab Chip*, 2019, **19**(18), 2973–2977.

36 J. Park and J. K. Park, Finger-Actuated Microfluidic Display for Smart Blood Typing, *Anal. Chem.*, 2019, **91**(18), 11636–11642.

37 P. Chen, *et al.*, Integrated and finger-actuated microfluidic chip for point-of-care testing of multiple pathogens, *Talanta*, 2021, **224**, 121844.

This journal is © The Royal Society of Chemistry 2025

Open Access Article. Published on 04 August 2025. Downloaded on 6/16/2026 10:50:35 PM.
This article is licensed under a Creative Commons Attribution-NonCommercial 3.0 Unported Licence.

38 M. Zimmermann, *et al.*, Capillary pumps for autonomous capillary systems, *Lab Chip*, 2007, **7**(1), 119–125.

39 A. O. Olanrewaju, *et al.*, Microfluidic Capillaric Circuit for Rapid and Facile Bacteria Detection, *Anal. Chem.*, 2017, **89**(12), 6846–6853.

40 A. Olanrewaju, *et al.*, Capillary microfluidics in microchannels: from microfluidic networks to capillaric circuits, *Lab Chip*, 2018, **18**(16), 2323–2347.

41 C. K. Byun, *et al.*, Pumps for microfluidic cell culture, *Electrophoresis*, 2014, **35**(2–3), 245–257.

42 P. M. Korczyk, *et al.*, Effects of unsteadiness of the rates of flow on the dynamics of formation of droplets in microfluidic systems, *Lab Chip*, 2011, **11**(1), 173–175.

43 J. R. Lake, K. C. Heyde and W. C. Ruder, Low-cost feedback-controlled syringe pressure pumps for microfluidics applications, *PLoS One*, 2017, **12**(4), e0175089.

44 Z. Li, C. Liu and J. Sun, Hydraulic-electric analogy for design and operation of microfluidic systems, *Lab Chip*, 2023, **23**(15), 3311–3327.

45 N. A. Filatov, *et al.*, Open-Source Pressure Controller Based on Compact Electro-Pneumatic Regulators for Droplet Microfluidics Applications, *IEEE Trans. Instrum. Meas.*, 2022, **71**, 1–10.

46 X. R. Wang, *et al.*, Microblower-based microfluidic pump, *Sens. Actuators, A*, 2017, **253**, 27–34.

47 Y. S. Bai, *et al.*, A handheld, wide-range pressure pump for portable microfluidic applications, *Sens. Actuators, A*, 2024, **377**, 115683.

48 H. W. Brown, Capillary Pressure Investigations, *J. Pet. Technol.*, 1951, **3**(3), 67–74.

49 A. Shakeri, S. Khan and T. F. Didar, Conventional and emerging strategies for the fabrication and functionalization of PDMS-based microfluidic devices, *Lab Chip*, 2021, **21**(16), 3053–3075.

50 H. Cho, *et al.*, How the capillary burst microvalve works, *J. Colloid Interface Sci.*, 2007, **306**(2), 379–385.

51 N. Atceken, *et al.*, Point-of-Care Diagnostic Platforms for Loop-Mediated Isothermal Amplification, *Adv. Eng. Mater.*, 2022, **25**(8), 2201174.

52 N. Atceken, D. Yigci, B. Ozdalgic and S. Tasoglu, CRISPR-Cas-Integrated LAMP, *Biosensors*, 2022, **12**(11), 1035.

53 N. Atceken, *et al.*, Development and Validation of LAMP Assays for Distinguishing MPXV Clades with Fluorescent and Colorimetric Readouts, *Biosensors*, 2025, **15**(1), 23.

54 Y. Li, *et al.*, Real-time PCR assays for the specific detection of monkeypox virus West African and Congo Basin strain DNA, *J. Virol. Methods*, 2010, **169**(1), 223–227.

55 N. Atceken, *et al.*, Development and Validation of LAMP Assays for Distinguishing MPXV Clades with Fluorescent and Colorimetric Readouts, *Biosensors*, 2025, **15**(1), 23.

56 Y. Yamauchi, *et al.*, What determines unique yellow, L/M cone ratio or visual experience? 9th Congress of the International Color Association, 2002, Vol. 4421, SPIE.

57 Y. Belotti and C. T. Lim, Microfluidics for Liquid Biopsies: Recent Advances, Current Challenges, and Future Directions, *Anal. Chem.*, 2021, **93**(11), 4727–4738.

58 J. Sun, *et al.*, An Integrated Micro-Heating System for On-Chip Isothermal Amplification of African Swine Fever Virus Genes, *Small*, 2024, **20**(47), e2402446.

59 D. Natsuhara, *et al.*, A sequential liquid dispensing method in a centrifugal microfluidic device operating at a constant rotational speed for the multiplexed genetic detection of foodborne pathogens, *RSC Adv.*, 2024, **14**(31), 22606–22617.

60 Y. Murano, *et al.*, Development of 3D-structured tilt capillary valve for lab-on-a-disc devices, *Microfluid. Nanofluid.*, 2025, **29**(3), 18.